Vacuum-Referred Binding Energies of Bismuth and Lanthanide Levels in $LiTaO_3$ Perovskite

Toward Designing Energy Storage Phosphor for Anti-Counterfeiting, X-Ray Imaging, and Mechanoluminescence

Lyu, Tianshuai; Dorenbos, Pieter

DOI
10.1002/lpor.202200304

Publication date
2022

Document Version
Final published version

Published in
Laser and Photonics Reviews

LASER & PHOTONICS REVIEWS

www.lpr-journal.org

Vacuum-Referred Binding Energies of Bismuth and Lanthanide Levels in $LiTaO_3$ Perovskite: Toward Designing Energy Storage Phosphor for Anti-Counterfeiting, X-Ray Imaging, and Mechanoluminescence

Tianshuai Lyu and Pieter Dorenbos*

Discovering UV-light or X-ray charged afterglow and storage phosphors with high charge carrier storage capacity remains challenging. Herein, a method is proposed by combining vacuum referred binding energy (VRBE) diagram construction and optimization of dopants' concentration and compound synthesis. The refined chemical shift model, optical spectroscopy, and thermoluminescence will be combined to construct the VRBE diagram of $LiTaO_3$ with the lanthanide and bismuth charge transition levels. Based on the constructed VRBE diagram of $LiTaO_3$, Bi^{3+}, and/or Ln^{3+} (Ln = Tb or Pr) doped $LiTaO_3$ will be studied. By combining Bi^{3+} with Tb^{3+}, Pr^{3+}, or Bi^{3+} itself, Bi^{3+} emerges to act as a ≈0.62 eV deep electron trap, while Tb^{3+}, Pr^{3+}, or Bi^{3+} acts as about 1.5 eV deep hole capturing and recombination centres. The VRBE in the Bi^{2+} $^2P_{1/2}$ ground state will be derived by thermoluminescence study. Proof-of-concept X-ray imaging, compression force distribution monitoring, and color-tailoring for anti-counterfeiting will be demonstrated by using the developed Bi^{3+} and/or Ln^{3+} doped $LiTaO_3$. This work promotes the understanding of trap level locations and on the trapping and release processes of charge carriers in Bi^{3+} and/or lanthanides doped inorganic compounds for rational design of new afterglow and storage phosphors.

1. Introduction

Persistent luminescence (afterglow) and storage phosphors are inorganic compounds which trap charge carriers in host defect traps after charging by high energy photons or ionizing radiation like γ-rays, X-rays, 254 nm UV-light, electrons, or β-rays.[1]Continuous photon emission from minutes to hours appears in afterglow phosphors after stopping excitation.[2] Intense optically stimulated emission emerges in storage phosphors when the stored charge carriers are liberated by optical stimulation.[3] Because of these features, afterglow and storage phosphors have applications in computed radiography (CR),[4] battery-free light dosimeter,[5] anti-counterfeiting,[6] and bio-imaging.[1a] Although many compounds have been tried, the state-of-the-art afterglow and storage phosphors are still $SrAl_2O_4:Eu^{2+},Dy^{3+}$[3b,7] and $BaFBr(I):Eu^{2+}$.[3a] One reason for a limited progress is that a compound often has many intrinsic defects and the charge carrier capturing and release processes are difficult to discuss and are often not clear. Another reason is that many compounds were explored in a trial and error method instead of by a deep and systemic study. There is a demand to develop a general method that can guide us to rational design and explore afterglow or storage phosphors more efficiently.[2a,8]

Generally, an afterglow or storage phosphor contains a compound host lattice, an electron trapping center, a hole trapping center, and the recombination center. The recombination center can be the electron or hole trapping center, which determines the emission wavelength from deep UV-C to infrared like 1.06 μm.[2b,9] The electron and hole capturing centers can be host-related intrinsic defect(s) or deliberately doped dopant(s). The duration time of charge carriers captured at traps is determined by the trapping depths of the charge carriers and their distribution at the crystal host lattice.[3c] In an afterglow phosphor a <≈0.7 eV deep charge carrier capturing center is required to yield thermally stimulated emission at room temperature (RT).[1c] In a storage phosphor a >≈1.0 eV deep charge carrier capturing center is required to avoid the liberation of charge carriers at RT. If scientists can rational design and adjust the trapping depths of charge carriers in inorganic compounds, more efficient exploration and development of afterglow or storage phosphors becomes possible.[10]

T. Lyu
Xiamen Key Laboratory of Optoelectronic Materials and Advanced Manufacturing
Institute of Luminescent Materials and Information Displays
College of Materials Science and Engineering
Huaqiao University
Xiamen 361021, China
E-mail: lv_tianshuai@126.com; lv_tianshuai@hqu.edu.cn

P. Dorenbos
Faculty of Applied Sciences
Department of Radiation Science and Technology
Delft University of Technology
Mekelweg 15, Delft 2629JB, The Netherlands

The ORCID identification number(s) for the author(s) of this article can be found under https://doi.org/10.1002/lpor.202200304

DOI: 10.1002/lpor.202200304

The chemical shift model was established in 2012 to construct a so-called vacuum referred binding energy (VRBE) diagram for lanthanides doped inorganic compounds.[11] One then can compare the electron binding at the conduction band (CB) bottom, the valence band (VB) maximum, or in the ground states of trivalent and divalent lanthanides in various crystals with respect to an identical energy, i.e., the vacuum level.[12] The chemical shift model was recently revised and updated,[13] which then makes the constructed VRBE more accurate to predict the level locations of lanthanides in inorganic compounds. Note that the Ln^{2+} ground state level location in a VRBE diagram has the same meaning as the $Ln^{2+/3+}$ charge transition level. The similar applies to Ln^{3+}, Bi^{3+}, and Bi^{2+}. Bi^{3+} and Bi^{2+} ions with the $6s^2$ and $6s^26p$ electron configurations have been largely explored as dopants in many inorganic compounds for phosphor based lighting. Compared with Eu^{2+} as a dopant, the Bi^{3+} or Bi^{2+} based afterglow and storage phosphors are rarely reported.[14] Awater et al. studied the spectroscopic data of Bi^{3+} in 117 inorganic compounds in ref. [15] where the VRBEs in the ground and excited states of Bi^{3+} were roughly determined and analyzed. Awater et al. also studied and roughly estimated the VRBEs in Bi^{2+} ground states in 15 compounds in ref. [16]. However, to the best of our knowledge, the VRBE diagram containing the level locations of lanthanides together with those of Bi^{3+} and Bi^{2+} are rarely reported and experimentally verified. This also means that it is interesting to use the VRBE diagram to explore new Bi^{3+} and/or lanthanides based afterglow and storage phosphors.

$LiTaO_3$ has a perovskite structure and crystallizes in a trigonal phase with R3c space group at room temperature. Because of a high density of about 7.45 g cm^{-3}, it has a high absorption coefficient of X-rays. This means that $LiTaO_3$ may be a good host to explore X-ray charged afterglow or storage phosphors. In 1996, emission and X-ray charged storage properties of Tb^{3+} doped $LiTaO_3$ was studied in ref. [17] where it remained unclear whether Tb^{3+} acts as a hole trapping center or not. In 2020, Hu et al. reported the persistent luminescence properties of Bi^{3+} doped $LiTaO_3$ after 254 nm UV-light charging in ref. [18] where whether Bi^{3+} acting as a charge carrier capturing center or not is not clear. In 2022, Li et al. reported the mechanoluminescence properties of Pr^{3+},Ca^{2+}/Si^{4+} co-doped $LiTaO_3$ in ref. [19] where whether Pr^{3+} acting as a hole capturing center or not is not clear. Very recently, we observed nice photochromism phenomenon in Bi^{3+},Dy^{3+}-doped $LiTaO_3$ in ref. [20] where charge carrier trapping and de-trapping processes are not fully clear. The VRBE diagram construction of $LiTaO_3$ will help us to identify and discuss the charge carrier trapping and release processes in $LiTaO_3$. To the best of our knowledge, the VRBE diagram of $LiTaO_3$ including the level locations of lanthanides, Bi^{3+}, and Bi^{2+} is not reported yet. The Bi^{3+} and/or Ln^{3+} (Ln = Tb, Pr, or Eu) doped $LiTaO_3$ compounds are not systematically studied for 254 nm UV-light or X-ray charged afterglow or storage phosphor applications. The mechanoluminescence is also not reported in the Bi^{3+},Pr^{3+}-co-doped $LiTaO_3$.

The objective of this work is to demonstrate how to develop afterglow and storage phosphors by combining vacuum referred binding energy (VRBE) diagram construction and optimization of dopants' concentration and compound synthesis. The refined chemical shift model, optical spectroscopy, and thermoluminescence will be combined to construct the VRBE diagram of $LiTaO_3$ as shown in **Figure 1**, which works as a basis for our study. The VRBEs in the Bi^{3+} $^1S_0$ ground state and in the Bi^{2+} $^2P_{1/2}$ ground state will be determined by spectroscopy and thermoluminescence study. The trapping and release processes of charge carriers in Bi^{3+} and/or Ln^{3+} doped $LiTaO_3$ will be studied by both the optical and mechanical stimulation. Proof-of-concept X-ray imaging, compression force distribution monitoring, and color-tailoring for anti-counterfeiting will be demonstrated by using the developed Bi^{3+} and/or Ln^{3+} doped $LiTaO_3$. This work promotes our understanding of trap level locations and on the trapping and release processes of charge carriers in Bi^{3+} and/or lanthanides doped inorganic compounds for rational design of new afterglow and storage phosphors.

2. Results

2.1. Photoluminescence Spectroscopy for VRBE Construction

Figure 2a,b shows the PLE and PL spectra of the undoped $LiTaO_3$ host, and Eu^{3+} or Bi^{3+} doped $LiTaO_3$ at RT. A broad excitation band peaked at ≈271.5 nm appears in the PLE spectrum of $LiTaO_3$:0.005Eu^{3+}, which will be assigned to electron transfer from the valence band to Eu^{3+} or the VB→Eu^{3+} charge transfer (CT) band. Upon 230 nm excitation, the undoped $LiTaO_3$ host shows several emission bands in the spectral range between 300 and 650 nm. An excitation band peaked at 226.5 nm (5.47 eV) appears in the excitation spectrum of the $LiTaO_3$ host when 375, 467, 555, or 590 nm emission was monitored as in Figure 2a and Figure S3 (Supporting Information), which will be assigned to host exciton creation at room temperature. Upon 300 nm excitation, $LiTaO_3$:0.005Bi^{3+} shows a broad emission band peaked at 440 nm (2.82 eV) in Figure 2b. Like in ref. [20], it is attributed to Bi^{3+} D-band emission. The excitation spectrum (λ_{em} = 437 nm) of $LiTaO_3$:0.005Bi^{3+} in Figure 2a shows an excitation band peaked at ≈253 nm and a broad band peaked at ≈299.5 nm.

To further unravel the Bi^{3+} luminescence in $LiTaO_3$, the PLE and PL spectra of $LiTaO_3$:0.005Bi^{3+} were measured at 10 K and shown in Figure 2c,d. Similar to Figure 2b, $LiTaO_3$:0.005Bi^{3+} shows a broad D-band emission peaked at 440 nm upon 301 nm excitation in Figure 2d. The excitation spectrum (λ_{em} = 440 nm) in Figure 2c shows a weak excitation band at ≈218 nm, a shoulder band at ≈260 nm, and an asymmetric band at ≈301 nm. The 301 nm band will be assigned to a combined contribution from the Bi^{3+} D-band and A-band.

Figure 2e and Figure S4 (Supporting Information) show the PLE and PL spectra of $LiTaO_3$:0.01Tb^{3+} recorded at RT. The RT excitation spectrum shows a broad excitation band peaked near 290 nm. Figure 2f shows the PLE and PL spectra of $LiTaO_3$:0.005Tb^{3+} measured at 10 K. A broad excitation band peaked at ≈285 nm appears. Other than Nikl et al. who assigned the band to Tb^{3+} 4f→5d transition in ref. [17], we will assign it to the Intervalence Charge Transfer Band (IVCT) induced by electron transfer from the 4f ground of Tb^{3+} to the conduction band (CB), i.e., IVCT Tb^{3+}→CB.[22] Such assignment agrees well with the VRBE diagram of Figure 1.

Figure 2g and Figure S5 (Supporting Information) show the PLE and PL spectra of $LiTaO_3$:0.01Pr^{3+} measured at RT. The RT excitation spectrum shows a broad excitation band peaked at ≈295 nm. Figure 2h shows the PLE and PL spectra of

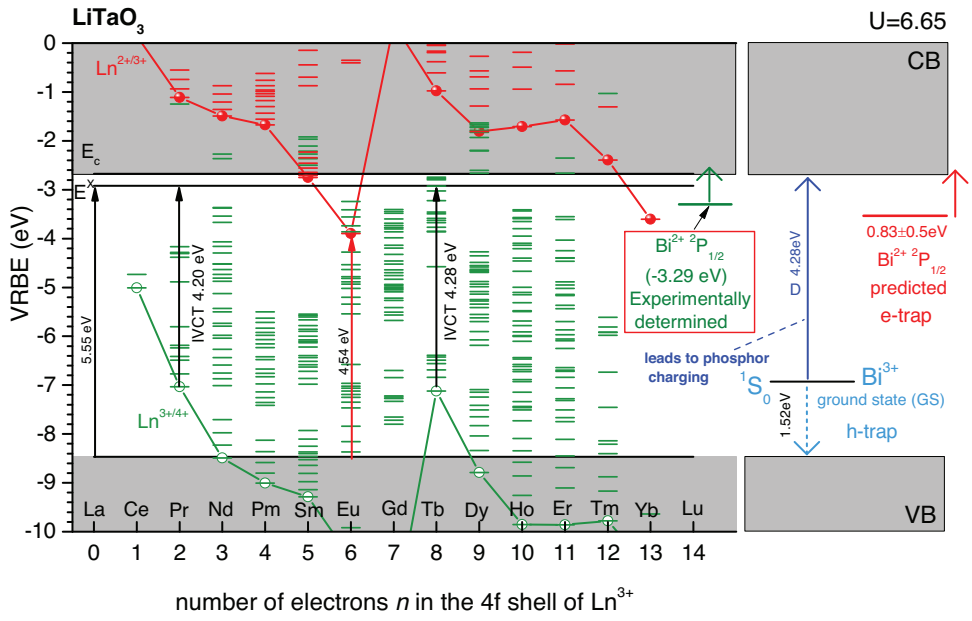

Figure 1. Vacuum referred binding energy (VRBE) diagram of $LiTaO_3$. The energy level locations of lanthanides, Bi^{2+}, and Bi^{3+} are shown. The experimentally observed transitions are illustrated by solid arrows.

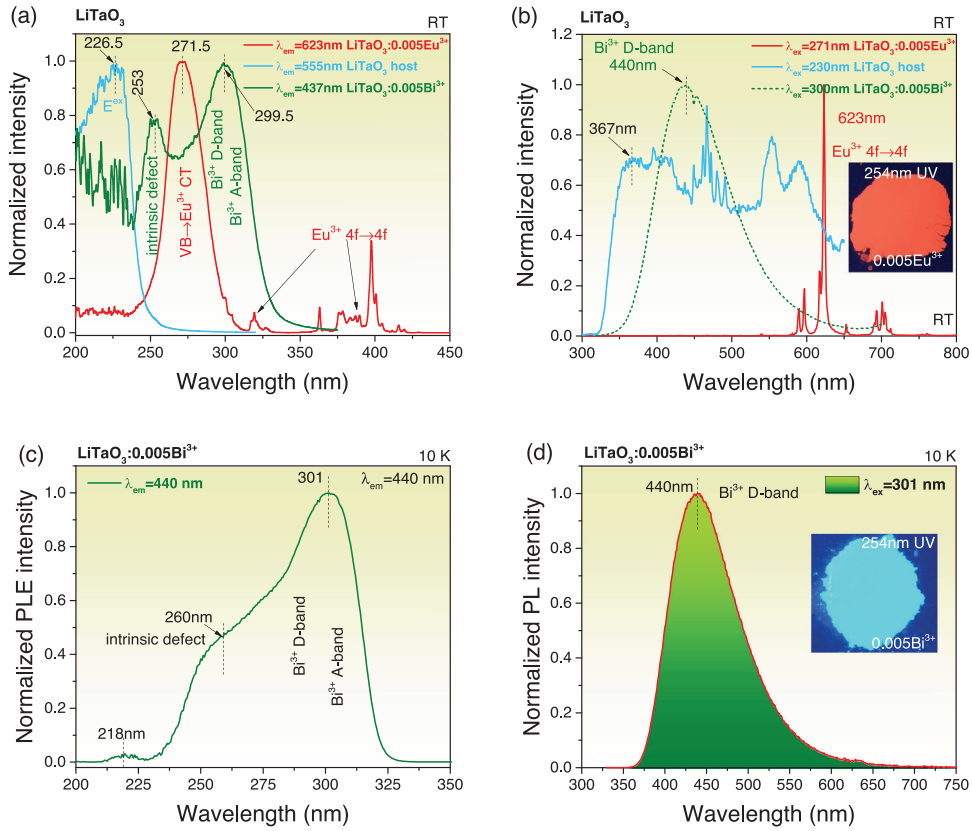

Figure 2. PLE and PL spectra of a,b) $LiTaO_3$ host, Eu^{3+} or Bi^{3+} doped $LiTaO_3$ recorded at RT, c,d) Bi^{3+} doped $LiTaO_3$ recorded at 10 K, Tb^{3+} or Pr^{3+} doped $LiTaO_3$ recorded at e,f) RT and g,h) 10 K, i) $LiTaO_3$ host recorded at 10 K, and j) $LiTaO_3$:0.005Bi^{3+},0.005Pr^{3+} recorded at RT. The insets are the photographs of Bi^{3+} and/or lanthanides doped $LiTaO_3$ under Hg lamp (254 nm UV-light) illumination at RT.

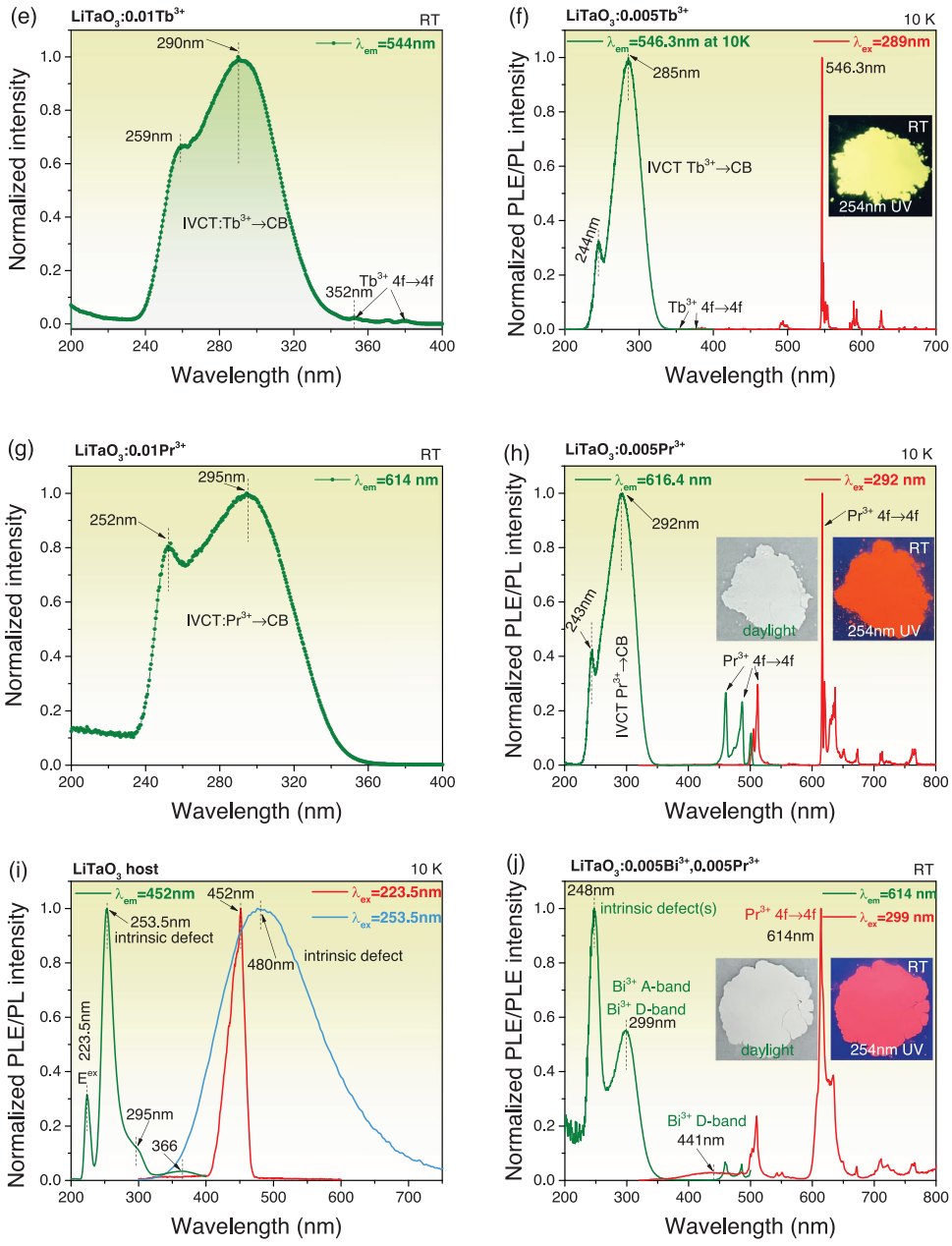

Figure 2. *Continued*

$LiTaO_3$:0.005Pr^{3+} measured at 10 K. Similar to Figure 2g, a broad excitation band peaked at 292 nm and several line excitation bands in 450–550 nm appear (λ_{em} = 616.4 nm). The line excitation bands are assigned to the Pr^{3+} 4f→4f transitions. The excitation spectrum in the spectral range between 200 and 400 nm for Tb^{3+} in Figure 2e,f is very similar to that for Pr^{3+} in Figure 2g,h. The broad excitation band peaked at ≈292 nm in Figure 2g,h was also observed by Qiu et al. in ref. [19b] and will be assigned to the Pr^{3+}→CB IVCT.

Figure 2i shows the PLE and PL spectra of the undoped $LiTaO_3$ host measured at 10 K. Four excitation bands peaked at 223.5, 253.5, 295, and 366 nm appear (λ_{em} = 452 nm). The 223.5 nm (5.55 eV) band will be assigned to host exciton creation at 10 K. The value was used in the VRBE diagram of Figure 1. An emission band peaked at 452 or 480 nm emerges in the spectral range from 300 to 750 nm upon 223.5 or 253.5 nm excitation at 10 K.

Figure 2j shows the PLE and PL spectra of $LiTaO_3$:0.005Bi^{3+},0.005Pr^{3+} recorded at RT. Similar to the PLE spectrum (λ_{em} = 437 nm) of $LiTaO_3$:0.005Bi^{3+} in Figure 2a, an excitation band peaked at 248 nm and a broad and asymmetric excitation band peaked at ≈299 nm appear (λ_{em} = 614 nm). Upon 290 nm excitation, a broad emission band peaked at 441 nm due to Bi^{3+} D-band emission and few characteristic Pr^{3+} 4f→4f emission peaks appear.

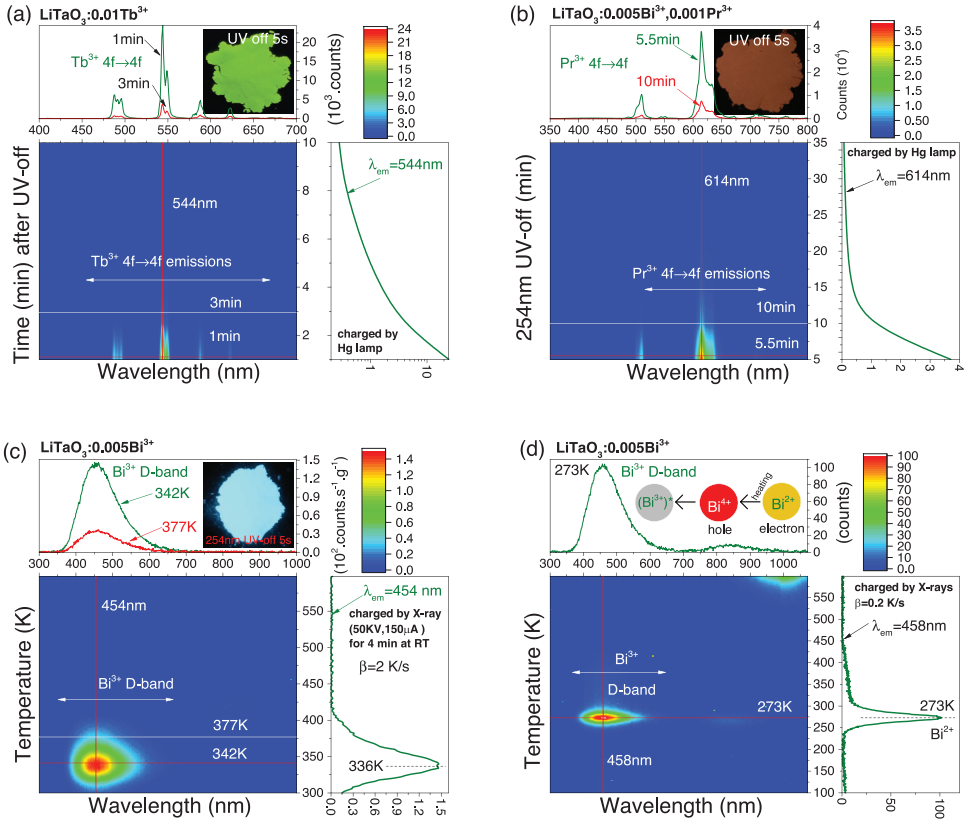

Figure 3. 2D contour plots of afterglow spectra as a function of time after exposure to 254 nm UV-light for a) $LiTaO_3$:0.01Tb^{3+} and b) $LiTaO_3$:0.005Bi^{3+},0.001Pr^{3+}. c) Above RT TLEM plot recorded at β = 2 K s^{-1} and d) above 100 K TLEM plot recorded at β = 0.2 K s^{-1} for $LiTaO_3$:0.005Bi^{3+} after exposure to X-rays. The insets in (a) until (c) show the afterglow photographs of the Bi^{3+} and/or Ln^{3+} (Ln = Tb or Pr) doped $LiTaO_3$ after 254 nm UV-light charging.

2.2. Evidencing the Electron Liberation Process from Bi^{2+}

To identify the recombination center, RT isothermal decay spectra and thermoluminescence emission (TLEM) spectra were measured. **Figure 3**a,b shows the RT isothermal decay spectra as a function of time for $LiTaO_3$:0.01Tb^{3+} and $LiTaO_3$:0.005Bi^{3+},0.001Pr^{3+} after 254 nm UV-light charging. Tb^{3+} and Pr^{3+} ions appear to act as the recombination centers. Figure 3c shows the above 300 K TLEM spectra recorded at a heating rate (β) of 2 K s^{-1} of $LiTaO_3$:0.005Bi^{3+} after exposure to X-rays. A TL glow curve peaked at 336 K with broad D-band emission in the spectral range from 350 to 700 nm is observed. Figure 3d shows the above 100 K TLEM spectra recorded at β = 0.2 K s^{-1} of $LiTaO_3$ after X-ray charging. A TL glow curve peaked at 273 K with typical Bi^{3+} D-band emission appears.

To study the electron release process from Bi^{2+}, low-temperature TL glow curves were measured. **Figure 4** shows the above 100 K TL glow curves of Bi^{3+} and/or Ln^{3+} (Ln = Tb or Pr) doped $LiTaO_3$ samples after exposure to X-rays at 93 K with a duration of 300 s. The ratios of the integrated TL intensity from 100 to 450 K of Bi^{3+} and/or Ln^{3+} doped $LiTaO_3$ to that of $LiTaO_3$:0.005Bi^{3+} are listed in the legend of Figure 4. All samples share a common TL glow peak near 164 K, which will be assigned to host-related intrinsic defect(s) in $LiTaO_3$. Compared with $LiTaO_3$:0.005Tb^{3+}, the Bi^{3+} co-doping in

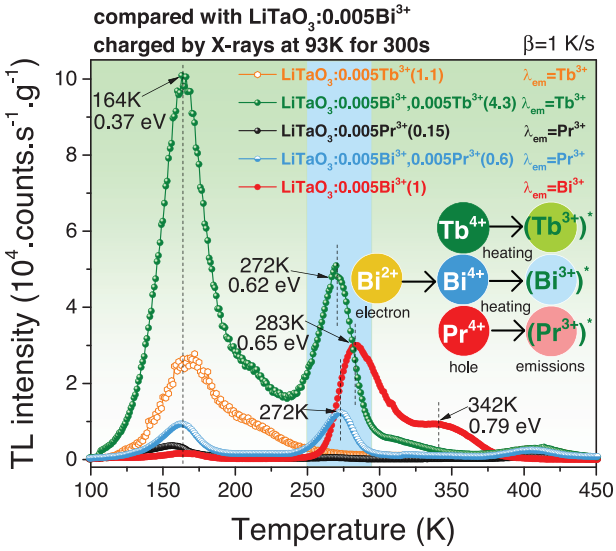

Figure 4. Above 100 K TL glow curves for Bi^{3+} and/or Ln^{3+} doped $LiTaO_3$ after X-ray charging at ≈93 K. The Tb^{3+}, Pr^{3+}, or Bi^{3+} emissions were monitored and the used heating rate was 1 K s^{-1}.

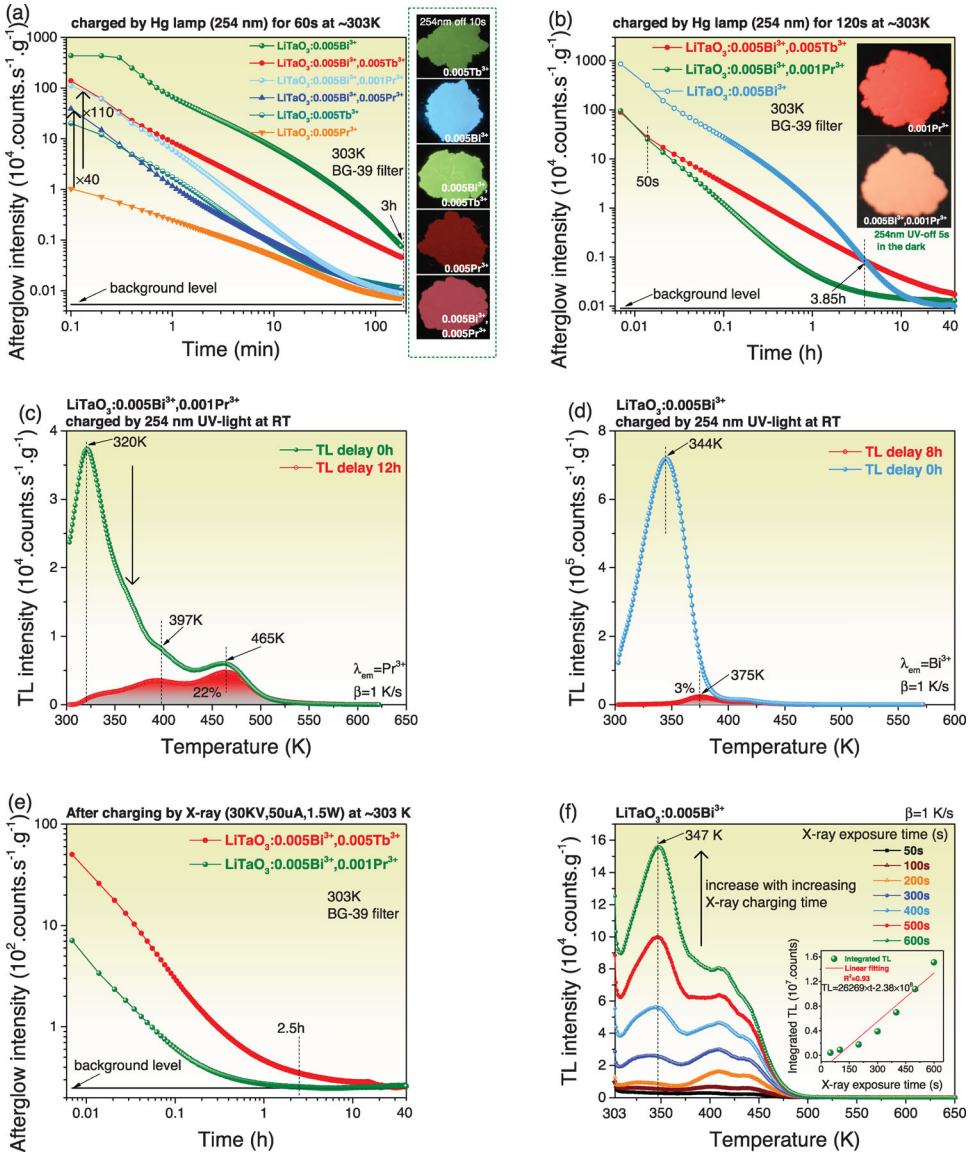

Figure 5. a,b) RT isothermal decay curves of Bi^{3+} and/or Ln^{3+} doped $LiTaO_3$ after exposure to 254 nm UV-light and fading of TL glow curves of c) $LiTaO_3$:0.005Bi^{3+}, 0.001Pr^{3+} and d) $LiTaO_3$:0.005Bi^{3+}. e) RT iso-thermal decay curves of $LiTaO_3$:0.005Bi^{3+},0.001Pr^{3+} and $LiTaO_3$:0.005Bi^{3+},0.005Tb^{3+} after exposure to X-rays. f) TL glow curves of $LiTaO_3$:0.005Bi^{3+} after exposure to X-rays with different duration. The inset in (f) shows the integrated TL intensities between 303 and 650 K as a function of X-ray exposure time. The insets in (a) and (b) show the afterglow photographs of Bi^{3+} and/or Ln^{3+} doped $LiTaO_3$ after 254 nm UV-light charging.

$LiTaO_3$:0.005Bi^{3+},0.005Tb^{3+} induces a new and intense TL glow peak near 272 K where Tb^{3+} is the recombination and luminescence center. Compared with $LiTaO_3$:0.005Pr^{3+}, the Bi^{3+} co-doping also induces a same TL peak near 272 K where Pr^{3+} is the recombination and luminescence center. TL glow peaks near 283 and 342 K appear in $LiTaO_3$:0.005Bi^{3+} in Figure 4 where the Bi^{3+} is the recombination and luminescence center. Considering the trap depth distribution in $LiTaO_3$:0.005Bi^{3+} (Figure S16, Supporting Information), the TL glow peak near 342 K of $LiTaO_3$:0.005Bi^{3+} in Figure 4 is consistent with that observed in the temperature from 303 to ≈400 K in Figure S6c,d6. The TL peak near 283 K of $LiTaO_3$:0.005Bi^{3+} in Figure 4 is close to the new 272 K TL peak as observed in $LiTaO_3$:0.005Bi^{3+},0.005Tb^{3+} and $LiTaO_3$:0.005Bi^{3+},0.005Pr^{3+}. The trap depths of the 272 and 283 K TL glow peaks were estimated to be 0.62 and 0.65 eV, as also indicated in Figure 4, by using Equation (S1) (Supporting Information) with T_m, $s = 3 \times 10^{10}$ s^{-1}, and $\beta = 1$ K s^{-1}. Both the 272 and 283 K TL glow peaks will be discussed and assigned to the thermally stimulated electron liberation from Bi^{2+} and recombination with holes captured at Bi^{4+}, Pr^{4+}, or Tb^{4+}, leading to characteristic Bi^{3+} D-band, Pr^{3+}, or Tb^{3+} 4f→4f emissions as illustrated in the inset of Figure 4.

Figure 5a shows the RT isothermal decay curves of Bi^{3+} and/or Ln^{3+} (Ln = Tb or Pr) doped $LiTaO_3$ after 254 nm UV-light charging. More than 3 h afterglow is measurable in all Bi^{3+} and/or Ln^{3+} doped $LiTaO_3$. Compared with Tb^{3+} or Pr^{3+} single doped $LiTaO_3$,

the Bi^{3+} co-doping greatly increases the afterglow intensity in $LiTaO_3$:0.005Bi^{3+},0.005Pr^{3+} and $LiTaO_3$:0.005Bi^{3+},0.005Tb^{3+}. Figure 5b shows that more than 40 h afterglow is measurable in $LiTaO_3$:0.005Bi^{3+}, $LiTaO_3$:0.005Bi^{3+},0.005Tb^{3+}, and the optimized $LiTaO_3$:0.005Bi^{3+},0.001Pr^{3+} after 254 nm UV-light charging.

Figure 5c,d shows the TL glow curves of $LiTaO_3$:0.005Bi^{3+},0.001Pr^{3+} and $LiTaO_3$:0.005Bi^{3+} after 254 nm UV-light charging followed by 12 or 8 h delay prior to TL readout. 78% or 97% of stored charge carriers in $LiTaO_3$:0.005Bi^{3+},0.001Pr^{3+} or $LiTaO_3$:0.005Bi^{3+} have been liberated at RT during 12 or 8 h delay time after 254 nm UV-light charging. Figure 5e shows the RT isothermal decay curves of $LiTaO_3$:0.005Bi^{3+},0.001Pr^{3+} and $LiTaO_3$:0.005Bi^{3+},0.005Tb^{3+} after X-ray charging. About 2.5 or 20 h afterglow is measurable in $LiTaO_3$:0.005Bi^{3+},0.001Pr^{3+} and $LiTaO_3$:0.005Bi^{3+},0.005Tb^{3+}.

Figure 5f shows the TL glow curves of $LiTaO_3$:0.005Bi^{3+} after X-ray charging with a duration from 50 to 600 s. The integrated TL intensity from 303 to 650 K as shown in the inset of Figure 5f, appears to increase with increasing X-ray charging time. Longer afterglow time is expected in Figure 5e by increasing X-ray exposure time. Possibly the developed $LiTaO_3$:0.005Bi^{3+} can be used as a dosimeter for X-ray detection.

To unravel charge carrier trapping processes, TL excitation (TLE) plots for Bi^{3+} and/or Ln^{3+} (Ln = Tb or Pr) doped $LiTaO_3$ were measured. **Figure 6**a shows the RT isothermal decay curves of $LiTaO_3$:0.005Bi^{3+} charged by different energy photon. The TLE plots for other Bi^{3+} and/or Ln^{3+} doped $LiTaO_3$ can be found in Figures S8, S12, and S19 (Supporting Information). Figure 6b–e compare the TLE plots with the PLE spectra of Bi^{3+} and/or Ln^{3+} doped $LiTaO_3$. The phosphors appear to be charged through the host related intrinsic defect(s), Bi^{3+} D-, and A-band, or Ln^{3+}→CB IVCT (Ln = Tb or Pr) optical excitation.

2.3. Designing Afterglow Phosphors for Anti-Counterfeiting, Mechanoluminescence, and X-Ray Imaging Applications

Charge carrier release processes were studied in Bi^{3+} and/or Ln^{3+} doped $LiTaO_3$ for developing new phosphors for anti-counterfeiting, mechanoluminescence, or X-ray imaging applications. **Figure 7**a,b shows the TL glow curves of $LiTaO_3$:0.005Bi^{3+} after 254 nm UV-light or X-rays charging followed by different energy photon stimulation. The ratios of the integrated TL intensities from 303 to 600 K with additional optical stimulation to that only with 254 nm UV-light or X-ray charging are listed in the legend of Figure 7a,b,e. The stored charge carriers in $LiTaO_3$:0.005Bi^{3+} appear to be efficiently released by wide range energy photon stimulation from 365 nm UV-light to 850 nm infrared laser. The same applies to $LiTaO_3$:0.005Bi^{3+},0.005Pr^{3+} in Figure 7e. Figure 7c1 shows the RT isothermal decay curves of $LiTaO_3$:0.005Bi^{3+} after X-ray charging and with a 850 nm laser stimulation from 60 to 180 s. Intense 850 nm stimulated emission appears when the stored charge carriers are rapidly liberated and weaker afterglow emerges in the 850 nm infrared light stimulated phosphor area. This phenomenon was used to show an afterglow symbol "O" with a 656 nm red laser stimulation as shown in Figure 7d4.

Figure 7f shows the TL glow curves of $LiTaO_3$:0.005Bi^{3+},0.005Pr^{3+} after first 254 nm UV-light charging and then ground in agate mortar with a duration from 0 until 300 s. The ratios of the integrated TL intensities from 303 to 600 K with grinding in agate mortar to that only with 254 nm UV-light charging are shown in the legend of Figure 7f. The stored charge carriers are gradually liberated with increasing grinding time from 0 to 300 s. Note that a weak new TL glow peak at ≈498 K appears with grinding in Figure 7f.

Figure 7g1 shows the TL glow curve of $LiTaO_3$:0.005Bi^{3+},0.005Pr^{3+} charged only by 600 s grinding in agate mortar. Compared with X-ray or 254 nm UV-light charging in Figure 7g2,g3, two new TL glow peaks near 504 and 588 K appear after 600 s grinding.

Figure 8a compares the 1000 N compression force induced emission spectra, also known as mechanoluminescence (ML) spectra, of $LiTaO_3$:0.01Pr^{3+} and $LiTaO_3$:0.005Bi^{3+},0.005Pr^{3+} based cylinders. Characteristic Pr^{3+} 4f→4f emissions appear in the spectral range from 300 to 1000 nm in $LiTaO_3$:0.005Bi^{3+},0.005Pr^{3+}. Figure 8b shows the ML spectra of $LiTaO_3$:0.005Bi^{3+},yPr^{3+} (y = 0.0005–0.012) based cylinders upon 1000 N compression force. The integrated ML intensities from 300 to 1000 nm are shown in the inset of Figure 8b. The y = 0.006 sample shows the strongest ML intensity. Figure 8c shows the ML photographs of y = 0.006 sample during 0 until 2000 N compression force loading in the dark.

Proof-of-concept colour tailoring for anti-counterfeiting application was explored by using the Bi^{3+} and/or Ln^{3+} (Ln = Tb or Pr) doped $LiTaO_3$. **Figure 9**a1–a4, Figures S18 and S21 (Supporting Information) show that the afterglow colour can be adjusted from red to yellow by increasing the Pr^{3+} concentration (y) from 0.001 to 0.012 in $LiTaO_3$:0.005Bi^{3+},yPr^{3+}. Figure 9b2 shows that a red afterglow text of "Bi^{3+}" appears in the dark by using the $LiTaO_3$:0.005Bi^{3+},0.001Pr^{3+} afterglow phosphor based film in Figure 9b1. The brightness of the afterglow "Bi^{3+}" text can be rapidly reduced by 2 s WLED stimulation as demonstrated in Figure 9b3,b4. The green or cyan afterglow from the 254 nm UV-light charged $LiTaO_3$:0.005Bi^{3+},0.005Tb^{3+} in Figure 9c2 or $LiTaO_3$:0.005Bi^{3+} in Figure 9d2 can be used as a backlight to display a QR code in Figure 9c3,d3 in the dark. The QR code can be scanned by a mobile phone to read out the hidden information of "Dr. Tianshuai Lyu for afterglow, storage, and mechanoluminescence research" in Figure 9d4.

The optimized $LiTaO_3$:0.005Bi^{3+} afterglow phosphor was dispersed in silicone gel to make a film 1 as shown in **Figure 10**a1 for X-ray imaging. A bright cyan afterglow film 1 appears in the dark after 254 nm UV-light charging in Figure 10a2. Figure 10a3 illustrates that the synthesized afterglow film 1 is flexible by hand bending. A metal spring was placed inside a plastic capsule. The metal spring is not visible during daylight since the plastic capsule is not transparent. The film 1 was placed underneath the plastic capsule as illustrated in Figure 10b1, which was then charged by X-rays at RT. Two X-ray imaging photographs appear in the dark by the thermally stimulated Bi^{3+} emission from the optimized $LiTaO_3$:0.005Bi^{3+} at RT (Figure 10b2) and at 340 K (Figure 10b3). The inset in Figure 10b3 shows the TL glow curves at β = 1 K s^{-1} for the optimized $LiTaO_3$:0.005Bi^{3+} and the state-of-the-art BaFBr(I):Eu^{2+} after X-ray charging. The ratio of the integrated TL intensity from 300 to 700 K of $LiTaO_3$:0.005Bi^{3+} to that

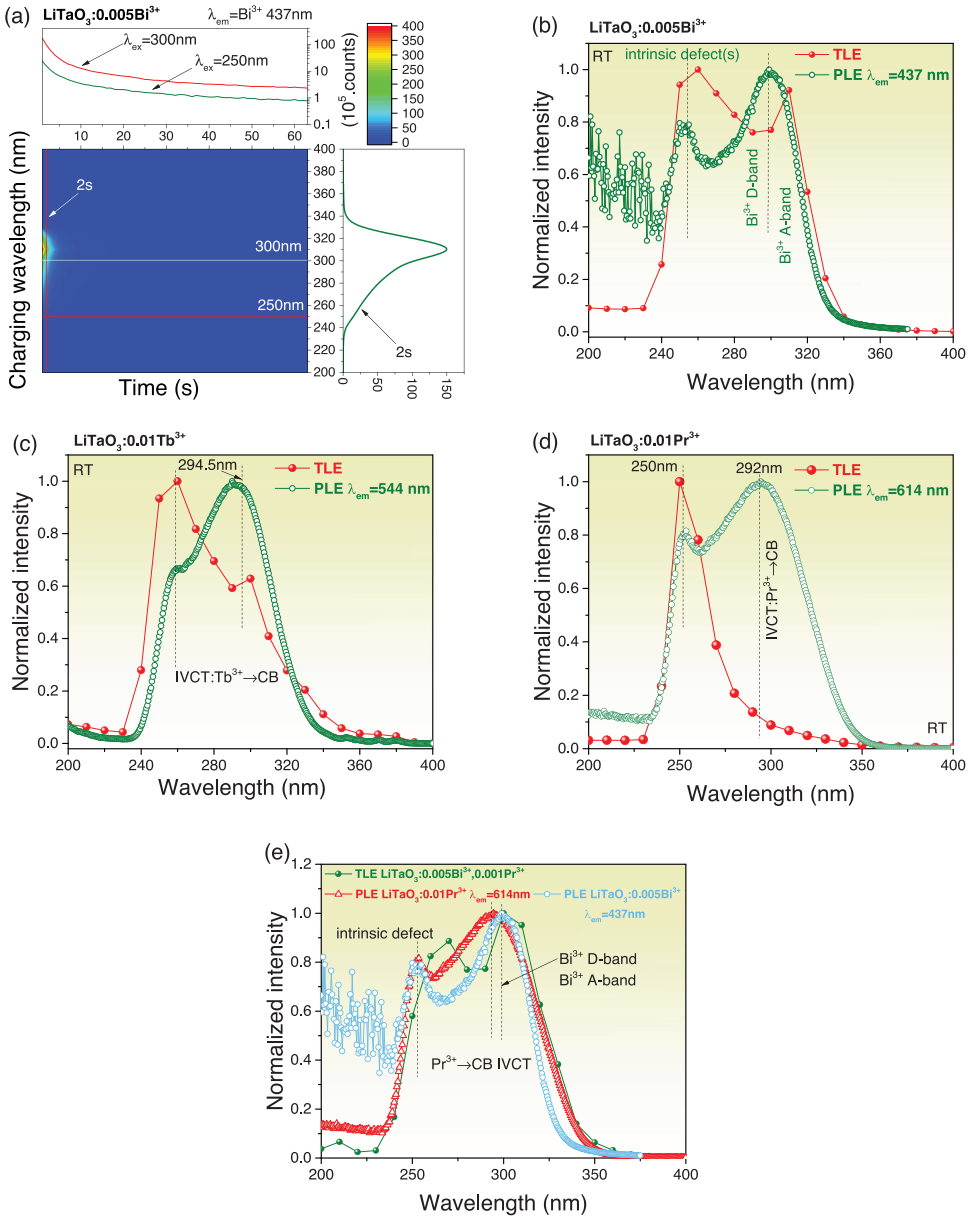

Figure 6. a) 2D contour plot of RT isothermal decay curves of $LiTaO_3$:0.005Bi^{3+} after exposure to different energy photon charging in the range between 200 and 400 nm. b–e) A comparison of the photoluminescence excitation spectra (PLE) and the thermoluminescence excitation (TLE) plots for Bi^{3+} and/or Ln^{3+} (Ln = Tb or Pr) doped $LiTaO_3$. The legends provide the monitored emission wavelengths for the PLE spectra.

of BaFBr(I):Eu^{2+} is about 2. The X-ray imaging resolution has been determined to be about 20 lp mm^{-1} for a $LiTaO_3$:0.005Bi^{3+} based silicone gel film as shown in Figure S26 (Supporting Information).

3. Discussion

3.1. Vacuum Referred Binding Energy (VRBE) Diagram of $LiTaO_3$

To analyze the trapping and release processes of charge carriers in $LiTaO_3$ perovskite, the VRBE diagram of $LiTaO_3$ will be first constructed and exploited. The VRBE of an electron denotes the energy required to extract that electron from a system, like the 4f ground state level of lanthanides in a compound, to the vacuum. The energy at rest in vacuum is then referred to as the zero point energy.[11,22b] A unique feature of the VRBE diagram is that the binding energy of an electron in a system like the conduction band (CB) bottom, valence band (VB) top, or 4f ground states of lanthanides can be compared in various compounds with respect to an identical energy reference.[10,23]

Figure 2a and Figure S3 (Supporting Information) shows that all the monitored emissions from 375 to 590 nm share a common excitation band peaked at ≈226.5 nm in the RT PLE spectra of the undoped $LiTaO_3$ host. A similar excitation band peaked at 223.5 nm appears in the 10 K PLE spectrum (λ_{em} = 452 nm) of the $LiTaO_3$ host. The excitation band peaked at ≈223.5 nm

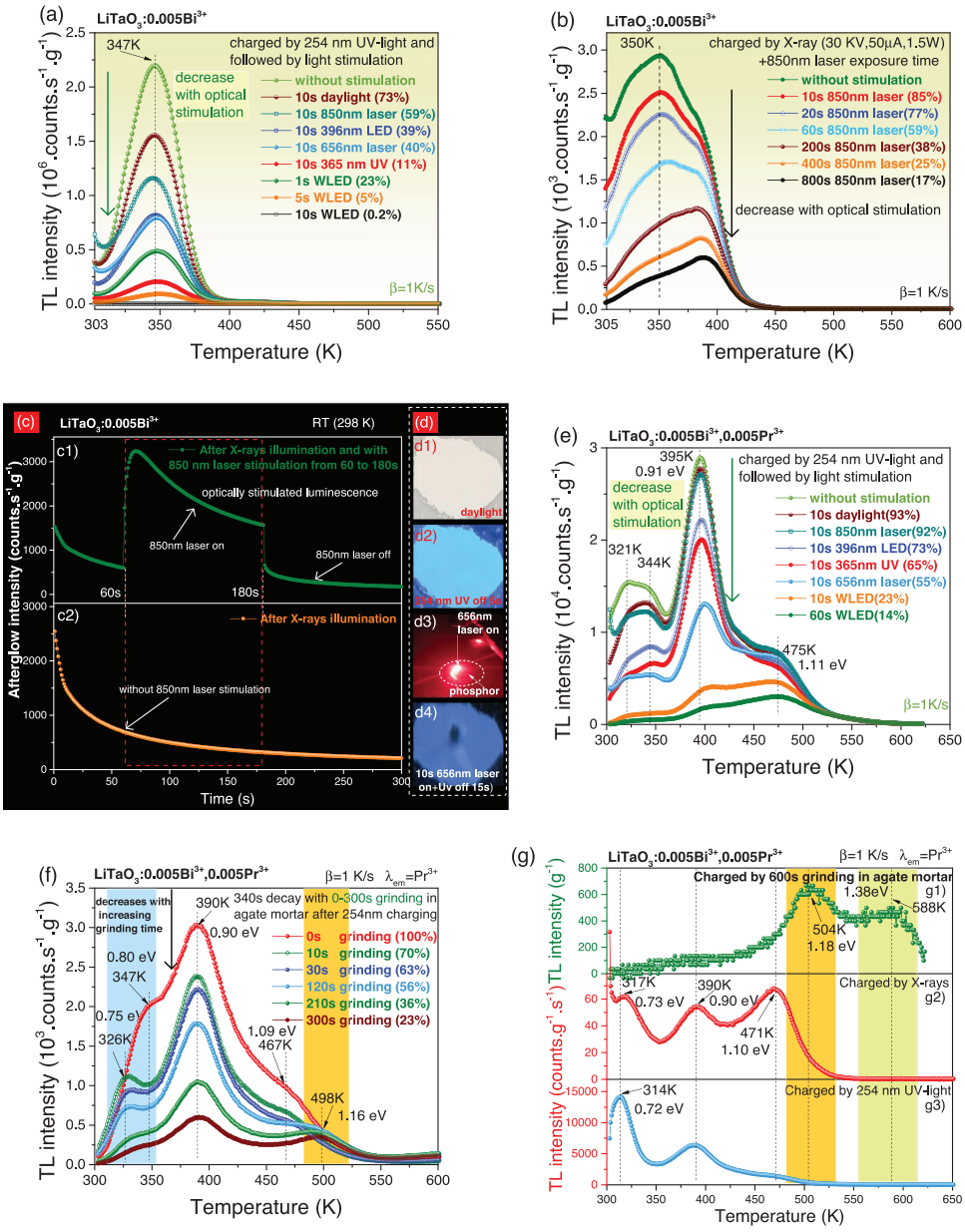

Figure 7. TL glow curves at $\beta = 1$ K s^{-1} after exposure to 254 nm UV-light or X-rays then followed by a) different energy photon stimulation or b) with 850 nm laser stimulation with 0 until 800 s duration time, and c) RT isothermal decay curves charged first by X-rays and then stimulated by 850 nm laser from 60 to 180 s for $LiTaO_3$:0.005Bi^{3+}. d) Information display of "O" by using the Bi^{3+} persistent luminescence and the optically stimulated emission behaviour in $LiTaO_3$:0.005Bi^{3+}. TL glow curves of $LiTaO_3$:0.005Bi^{3+},0.005Pr^{3+} after exposure to 254 nm UV-light then followed by e) different energy photon stimulation or with f) grinding in agate mortar with 0 until 300 s duration time. g) A comparison of TL glow curves of $LiTaO_3$:0.005Bi^{3+},0.005Pr^{3+} charged by g1) 600 s grinding in agate mortar, g2) X-rays, or with g3) 254 nm UV-light.

(5.55 eV) is therefore assigned to the host exciton creation. The excitation band ($\lambda_{em} = 623$ nm) peaked at ≈271.5 (4.57 eV) nm in the PLE spectrum of $LiTaO_3$:0.005Eu^{3+} in Figure 2a is consistent with that observed in ref. [24], which is then assigned to the O^{2-} to Eu^{3+} charge transfer (CT) band. The energy for electron transfer from the 4f ground states of Ln^{3+} (Ln = Tb or Pr) to the conduction band bottom was exploited to check the VRBE diagram of $LiTaO_3$. This transition is called the intervalence charge transfer (IVCT),[22,25] and it often appears in compounds where the conduction band bottom is lower than the lowest 5d levels of Ln^{3+} (Ln = Tb or Pr), like in $NaYGeO_4$, $NaLuGeO_4$,[22a] or $LuNbO_4$.[26] IVCT from the Ln^{3+} (Ln = Tb or Pr) not only provides information about the positions of the Ln^{3+} 4f ground states with respect to the CB-bottom, but also indicates that the Ln^{3+}-doped $LiTaO_3$ afterglow phosphors can be charged via the IVCT excitation. Figure 2e–h shows the PLE spectra of the Tb^{3+} or Pr^{3+} doped $LiTaO_3$ recorded at RT or 10 K. Two broad excitation bands peaked at ≈290 nm (4.28 eV) in Figure 2e,f and near 293 nm (4.23 eV)

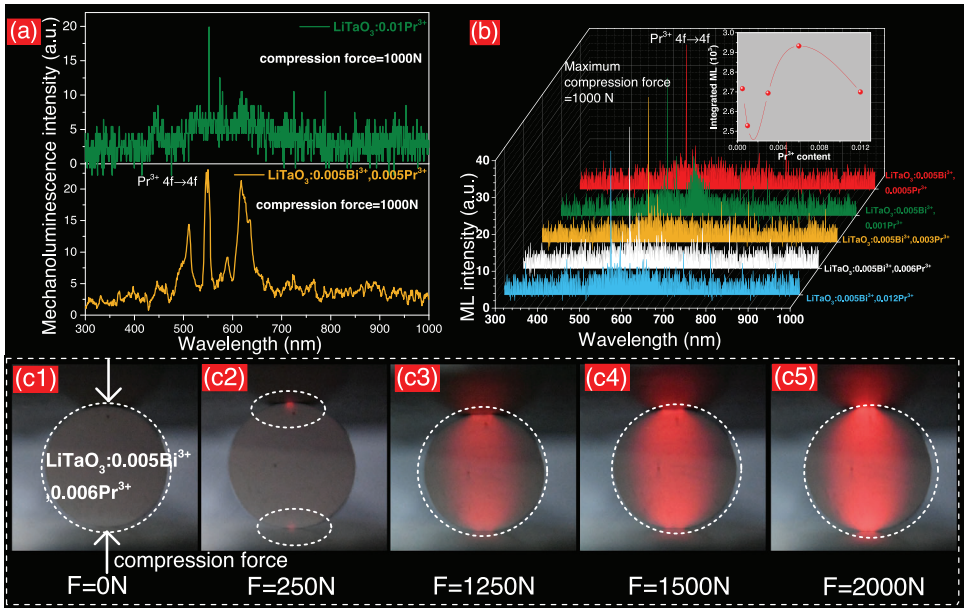

Figure 8. Mechanoluminescence spectra of a) $LiTaO_3$:0.01Pr^{3+} and $LiTaO_3$:0.005Bi^{3+},0.005Pr^{3+}, and b) $LiTaO_3$:0.005Bi^{3+},yPr^{3+} (y = 0.0005–0.012) based cylinders under 1000 N compression force. c) Mechanoluminescence photographs of $LiTaO_3$:0.005Bi^{3+},0.006Pr^{3+} under different compression force stimulation.

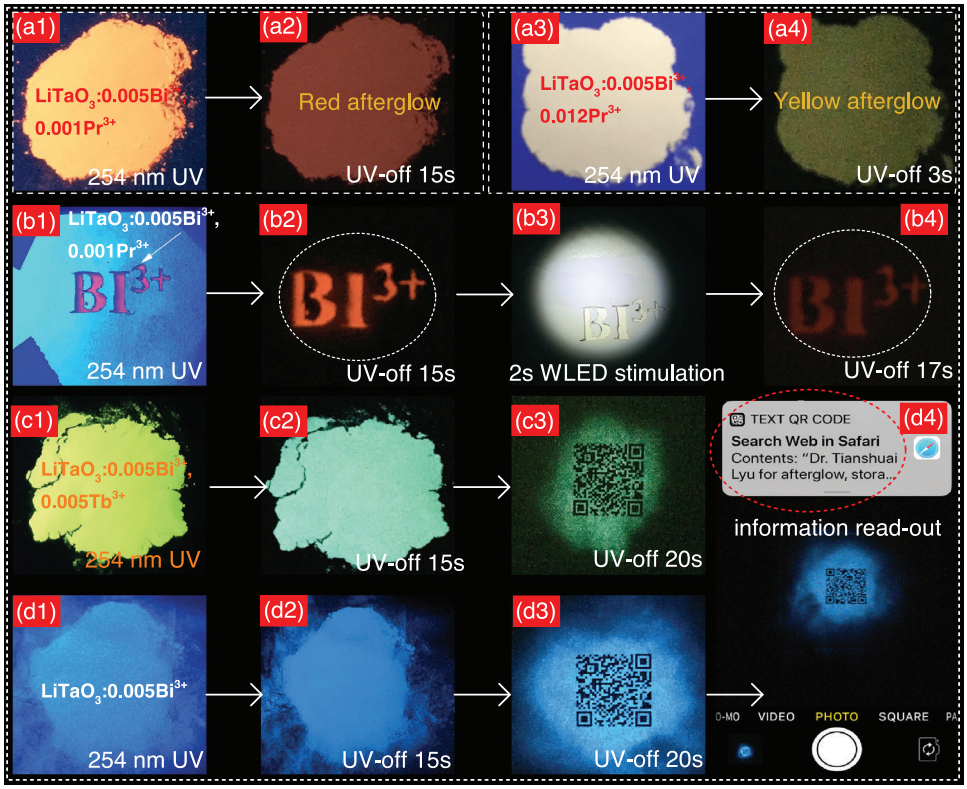

Figure 9. Proof-of-concept colour tailoring for anti-counterfeiting applications by using Pr^{3+}, Tb^{3+}, or Bi^{3+} afterglow from Bi^{3+} and Ln^{3+} co-doped $LiTaO_3$. a1–a4) Afterglow colour changes from red in $LiTaO_3$:0.005Bi^{3+},0.001Pr^{3+} to yellow in $LiTaO_3$:0.005Bi^{3+},0.012Pr^{3+}. b1–b4) Text display of "Bi^{3+}" by using the red afterglow from $LiTaO_3$:0.005Bi^{3+}, 0.001Pr^{3+}. QR code display by using the Tb^{3+} or Pr^{3+} afterglow from c1–c3) $LiTaO_3$:0.005Bi^{3+},0.005Tb^{3+} or d1–d4) $LiTaO_3$:0.005Bi^{3+} in the dark.

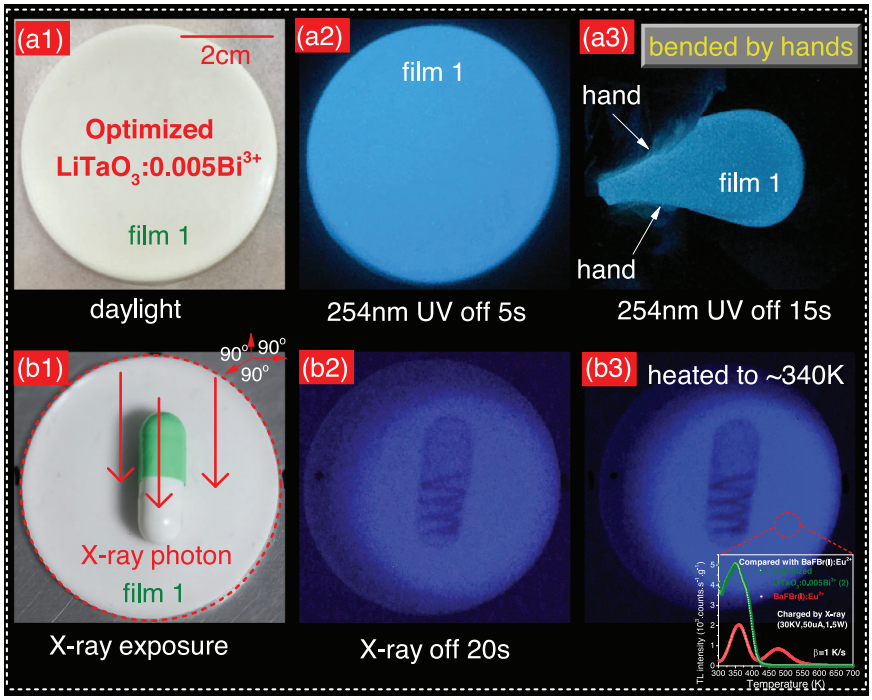

Figure 10. Proof-of-concept information storage by using the optimized $LiTaO_3$:0.005Bi^{3+}. a1–a3) Bi^{3+} afterglow from the flexible $LiTaO_3$:0.005Bi^{3+} afterglow phosphor dispersed in a silicone gel film. b1–b3) X-ray image of a capsule with metal by using the $LiTaO_3$:0.005Bi^{3+} based film after exposure to X-rays. The inset in (b3) shows the TL glow curves recorded at $\beta = 1$ K s^{-1} for the optimized $LiTaO_3$:0.005Bi^{3+} and the commercial BaFBr(I): Eu^{2+} after exposure to X-rays.

in Figure 2g,h were observed. Figure 6c,d demonstrates that the $LiTaO_3$:0.01Tb^{3+} and $LiTaO_3$:0.01Pr^{3+} afterglow phosphors can be charged through the two broad excitation bands near 293 nm. It means that free mobile electrons are formed in the conduction band of $LiTaO_3$ through the Ln^{3+}→CB IVCT excitation (Ln = Tb or Pr), which then fill the traps in Ln^{3+}-doped $LiTaO_3$. The broad excitation band peaked at ≈293 nm was therefore assigned to the intervalence charge transfer (IVCT) from the Ln^{3+} (Ln = Tb or Pr) ground state to the conduction band bottom of $LiTaO_3$. For the VRBE construction, an U parameter is required, which is equal to the ground state energy difference between Eu^{3+} and Eu^{2+}.[11] Herein, the U-value for $LiTaO_3$ was estimated to be ≈6.65 eV by using the weighted average electronegativity of the cations in $LiTaO_3$. With the above values for U, E^{ex}, E^{CT}, Pr(IVCT), and Tb(IVCT) a consistent VRBE diagram for $LiTaO_3$ containing the energy level locations of lanthanides is obtained as shown in Figure 1 by using the refined chemical shift model.[13,27]

3.2. VRBE at Bi^{3+} $^1S_0$ Ground State in $LiTaO_3$

Figure 2c,d shows the PLE and PL spectra of $LiTaO_3$:0.005Bi^{3+} recorded at 10 K. The PLE spectrum (λ_{em} = 440 nm) in Figure 2c shows a weak excitation band at 218 nm, a shoulder band at ≈260 nm, and an asymmetric band at ≈300 nm. The excitation band peaked at 260 nm in Figure 2c also appears in $LiTaO_3$ host in Figure 2i, which is then assigned to host-related intrinsic defect(s) in $LiTaO_3$. Considering that the excitation band peaked at ≈300 nm (4.13 eV) in Figure 2c is broad and the traps can be filled through the optical excitation in this band in Figure 6b,e, it has been assigned to the Bi^{3+} D-band. Possibly the Bi^{3+} A-band is located somewhere underneath the Bi^{3+} D-band as illustrated in Figure 2c. Considering the large Stokes shift in Figure 2a,b and broad emission band nature of $LiTaO_3$:0.005Bi^{3+}, the broad emission band with a maximum at 440 nm (2.82 eV) in the spectral range from 300 to 700 nm is attributed to the Bi^{3+} D-band luminescence. The VRBE in the Bi^{3+} $^1S_0$ ground state in $LiTaO_3$ was derived to be ≈−6.95 eV by using the energy of the Bi^{3+} D-band as shown in Figure 1. The VRBE of the Bi^{3+} $^1S_0$ ground state in $LiTaO_3$ is consistent with the statistic results reported in ref. [15] where, with increasing U value, the $^1S_0$ VRBE decreases from about −5 to −10 eV.

3.3. Electron Release from Bi^{2+} to Deduce VRBE at Bi^{2+} $^2P_{1/2}$ in $LiTaO_3$

The VRBE in the Bi^{2+} $^2P_{1/2}$ ground state in 15 inorganic compounds was analyzed in ref. [16], and falls in the range from about −3.0 to 4.0 eV.[28] To establish the VRBE in the Bi^{2+} $^2P_{1/2}$ ground state in $LiTaO_3$, a thermoluminescence study has been carried out in Figures 3, 4, and 6. Assuming a Bi^{2+} VRBE of −3.5+/−0.5 eV, Figure 1 predicts that Bi^{3+} can act as an about 0.83 ± 0.5 eV deep electron trap, while Bi^{3+}, Tb^{3+}, and Pr^{3+} will act as ≈1.52, 1.34, and 1.43 eV deep hole capturing centers in $LiTaO_3$. Figure 4 shows the above 100 K TL glow curves of Bi^{3+} and/Ln^{3+} (Ln = Tb or Pr) doped $LiTaO_3$ after X-ray charging. Compared with Ln^{3+} single doped $LiTaO_3$, a new TL glow

peak near 272–283 K emerges in $LiTaO_3$:0.005Bi^{3+},0.005Tb^{3+}, $LiTaO_3$:0.005Bi^{3+},0.005Pr^{3+}, and $LiTaO_3$:0.005Bi^{3+} where the Tb^{3+}, Pr^{3+}, and Bi^{3+} act as the hole capturing and recombination centers in $LiTaO_3$. Its trapping depth is determined to be about 0.62 eV by using Equation (S1) (Supporting Information), which is consistent with the predicted 0.83 ± 0.5 eV for the Bi^{3+} electron trap. We then assign the 272–283 K TL glow peak to electron release from Bi^{2+} and recombination with holes trapped at Bi^{4+}, Tb^{4+}, or Pr^{4+}, leading to Bi^{3+} D-band emission and characteristic 4f→4f emissions of Tb^{3+} or Pr^{3+}. Based on the derived Bi^{3+} electron trapping depth, the VRBE in the Bi^{2+} $^2P_{1/2}$ ground state is experimentally determined to be about −3.29 eV.[16] The above RT TL glow peaks in Bi^{3+} and/or Ln^{3+} (Ln = Tb or Pr) doped $LiTaO_3$ in Figure S6c,d are then assigned to the host-related intrinsic defects.

3.4. Bi^{3+} and/or Ln^{3+} Doped $LiTaO_3$ for Anti-Counterfeiting, X-Ray Imaging, and Mechanoluminescence

Figure 5c,d, and Figure S20 (Supporting Information) show that intense TL glow peak near RT appears in Bi^{3+} and/or Ln^{3+} (Ln = Tb or Pr) doped $LiTaO_3$. Figure 4 shows that the Bi^{2+} TL glow band near 283 K is broad in the range from 250 to 325 K in Bi^{3+}-doped $LiTaO_3$. Also considering that there is a trap depth distribution in $LiTaO_3$:0.005Bi^{3+} as demonstrated in Figure S16 (Supporting Information), electron release from Bi^{2+} can partly contribute to the RT isothermal afterglow in Figure 5a,b,e after 254 nm UV-light or X-ray charging. By combining Bi^{3+} and host-related intrinsic defects as electron traps with Bi^{3+} and Ln^{3+} (Ln = Tb or Pr) as hole traps, color-tailorable afterglow for anti-counterfeiting application appears in Bi^{3+} and/or Ln^{3+} doped $LiTaO_3$ as demonstrated in Figure 9 and Figure S25 (Supporting Information). The integrated TL intensity of the $LiTaO_3$:0.005Bi^{3+} has been optimized for X-ray imaging as demonstrated in Figure 10, which is about 2 times higher than that of the commercial BaFBr(I):Eu^{2+} after X-ray charging. Figure 7a–e demonstrate that the stored charge carriers in $LiTaO_3$:0.005Bi^{3+} and $LiTaO_3$:0.005Bi^{3+},0.006Pr^{3+} can be liberated by optical stimulation from 365 nm UV (3.40 eV) to 850 nm (1.46 eV) infrared laser. One may further develop the readout of an X-ray imaging photograph by optical stimulated luminescence instead of by heating the X-ray charged storage phosphor based film.

Figure 8c1–c5 shows that the compression force distribution monitoring was achieved by using the mechanoluminescence from the $LiTaO_3$:0.005Bi^{3+},0.006Pr^{3+} based cylinder. Figure 7f shows the TL glow curves of $LiTaO_3$:0.005Bi^{3+},0.005Pr^{3+} after 254 nm UV-light charging followed by 0 until 300 s grinding in agate mortar. The TL glow peaks from 326 to 467 K gradually decrease with increasing grinding time from 0 to 300 s. It indicates that the mechanoluminescence is related to the liberated charge carriers in $LiTaO_3$:0.005Bi^{3+},0.005Pr^{3+} after force loading. Figure 7f also shows that a new TL glow peak at ≈498 K appears in $LiTaO_3$:0.005Bi^{3+},0.005Pr^{3+} after grinding. Figure 7g further demonstrates that two new TL glow peaks at 504 and 588 K appear in $LiTaO_3$:0.005Bi^{3+}, 0.005Pr^{3+} after only 600 s grinding in agate mortar. It means that there is a force induced storage of charge carrier in $LiTaO_3$:0.005Bi^{3+},0.005Pr^{3+}, which possibly can be used for stress recording.[29] At this stage, it is difficult to unravel the formation of free charge carriers in $LiTaO_3$:0.005Bi^{3+},0.005Pr^{3+} during grinding. Possibly free electrons and holes are yielded by a piezoelectricity or triboelectricity related excitation process during grinding.[30] A part of the free charge carriers are captured by intrinsic defects based traps. During TL-readout, liberation of these stored charge carriers then leads to TL glow peaks at ≈498 and ≈588 K in Figure 7f,g1.

4. Conclusions

A principle to design, synthesize, and optimize persistent luminescence and storage phosphors for anti-counterfeiting, X-ray imaging, and mechanoluminescence was explored by using vacuum referred binding energy (VRBE) diagram construction and optimization of dopants' concentration and compound synthesis. We have first combined the refined chemical shift model, optical spectroscopy, and thermoluminescence study to establish the VRBE diagram for $LiTaO_3$. The photoluminescence excitation and emission spectra of $LiTaO_3$ host, Eu^{3+}, Tb^{3+}, Pr^{3+}, or Bi^{3+} doped $LiTaO_3$ were studied at RT or 10 K. This was utilized to construct the VRBE diagram of $LiTaO_3$ containing the level locations of lanthanides and Bi^{3+}. The VRBE in the Bi^{3+} $^1S_0$ ground state was derived to be ≈−6.95. The constructed VRBE diagram helps us to deeply understand the charge carrier trapping and release processes and to discover new afterglow or storage phosphors. As a demonstration, Bi^{3+} and/or Ln^{3+} (Ln = Tb or Pr) doped $LiTaO_3$ were studied. By combining Bi^{3+} with Tb^{3+}, Pr^{3+}, or Bi^{3+} itself, Bi^{3+} appears to act a ≈0.62 eV deep electron trapping center, while Tb^{3+}, Pr^{3+}, or Bi^{3+} act as about 1.5 eV deep hole trapping and recombination centers. Upon heating at about 272 K, the electrons are liberated from Bi^{2+} to recombine with holes trapped at Bi^{4+}, Tb^{4+}, or Pr^{4+}, leading to Bi^{3+} D-band and typical 4f→4f emissions of Tb^{3+} or Pr^{3+}. The VRBE in the Bi^{2+} $^2P_{1/2}$ ground state is then experimentally determined to be ≈3.29 eV. Host-related intrinsic defects are also important for the above RT TL glow curves of Bi^{3+} and/or Ln^{3+} (Ln = Tb or Pr) doped $LiTaO_3$. The integrated TL intensities between 303 and 650 K of optimized $LiTaO_3$:0.005Bi^{3+},0.005Tb^{3+} and $LiTaO_3$:0.005Bi^{3+} is about 0.6 and 2 times higher than that of the commercial BaFBr(I):Eu^{2+} after X-ray charging. More than 40 h Bi^{3+}, Tb^{3+}, or Pr^{3+} afterglow is measureable in the optimized $LiTaO_3$:0.005Bi^{3+}, $LiTaO_3$:0.005Bi^{3+},0.005Tb^{3+}, and $LiTaO_3$:0.005Bi^{3+},0.001Pr^{3+} after 254 nm UV-light charging. The stored charge carriers in Bi^{3+} and/or Ln^{3+} doped $LiTaO_3$ can be liberated by optical stimulation from 365 nm UV-light to 850 nm infrared laser and also by mechanical stimulation. Particularly, force induced storage of charge carriers appears in $LiTaO_3$:0.005Bi^{3+},0.005Pr^{3+}. Proof-of-concept X-ray imaging, compression force distribution monitoring, and color-tailoring for anti-counterfeiting were demonstrated in the developed Bi^{3+} and/or Ln^{3+} doped $LiTaO_3$. This work not only reports 254 nm UV-light or X-ray charged Bi^{3+} and/or Ln^{3+} doped $LiTaO_3$ phosphors with good charge carrier storage, but also promotes our understanding of trap level locations and on the trapping and release processes of charge carriers in Bi^{3+} and/or lanthanides doped inorganic compounds for rational design of new afterglow and storage phosphors.

5. Experimental Section

All utilized chemicals were bought from Shanghai Aladdin chemical company and stored in a dry room. The lanthanides and/or bismuth doped $LiTaO_3$ compounds have been prepared by a typical high-temperature solid-state reaction technique. The appropriate stoichiometric mixture of Ta_2O_5 (99.99%), Li_2CO_3 (99.99%), Bi_2O_3 (99.99%), and rare earth oxides with a high purity of 4N (99.99%) were ground and mixed homogeneously in an agate mortar with the help of mortar pestle and acetone for about 15 min. The well mixed powder was placed in a covered alumina crucible and then was heated at 800 °C for 120 min and then at 1200 °C with a duration of 360 min in a tube furnace in ambient atmosphere. 3 °C min^{-1} was used as the heating rate for the furnace. The prepared compounds were cooled to room temperature (RT) and then ground and mixed well again before optical measurements. To demonstrate X-ray imaging application, a flexible film was fabricated by dispersing the $LiTaO_3$:0.005Bi^{3+} afterglow phosphor in silicone gel (Sylgard 184, Dow Corning). The phosphor was mixed well with the silicone gel and then uniformly placed on a polished sapphire substrate. The substrate with the film was then placed in vacuum and heated at ≈70 °C with a duration of 2 h. To study mechanoluminescence property, a hard cylinder with a diameter of 2.5 cm was made by dispersing ≈0.8 g $LiTaO_3$:0.005Bi^{3+},yPr^{3+} phosphor in ≈6.4 g epoxy resin. The mixture was then placed in a silicone gel based mold, which was then heated at 80 °C with a duration of 2 h in vacuum.

All prepared compounds were checked by using a Japan Rigaku Smar/SmartLa X-ray diffraction facility equipped with an X-ray tube at 40 kV and 30 mA. The scanning electron microscope (SEM) photograph for $LiTaO_3$:0.005Bi^{3+} afterglow phosphor was recorded by a Japan JEOL JSM-7610FPlus electron microscope. Room temperature (RT) afterglow spectra, RT isothermal afterglow decay curves, photoluminescence excitation spectra (PLE), and emission spectra (PL) were measured by using a commercial FLS920 fluorescence spectrometer (Edinburgh Instruments Ltd.). X-ray excited emission spectra, low temperature PLE, and PL spectra at about 10 K were recorded by a FLS980 fluorescence spectrometer (Edinburgh Instruments Ltd.), which contains a single photon counting R928P photomultiplier (Hamamatsu Ltd.), a closed helium cryostat, an X-ray tube, and a monochromator with a high resolution of 0.1 mm. The measured PLE spectra were corrected by the wavelength-dependent excitation intensity of the used xenon lamp. The recorded PL spectra were corrected by the quantum efficiency of the used photomultiplier. The afterglow photographs of the bismuth and/or lanthanides doped $LiTaO_3$ after Hg lamp (254 nm UV-light) charging were recorded with an iPhone 13Pro. The mechanoluminescence (ML) photographs of $LiTaO_3$:0.005Bi^{3+},0.005Pr^{3+} based cylinder with 0 until ≈2000 N compression force loading were recorded by a Nikon D850 camera. The mechanoluminescence spectra were measured by a spectrometer QE65000 (Ocean Optics) in the range from 300 to 1000 nm. Prior to ML measurements, the $LiTaO_3$:0.005Bi^{3+},yPr^{3+} ($y = 0.0005$ until 0.012) based cylinders were placed in the dark with a duration of 3 min after Hg lamp (WFH-204BS, Hangzhou Qiwei Instrument, Ltd.) charging.

Above 100 K thermoluminescence (TL) glow curves, TL emission (TLEM) spectra, above RT TL glow curves, RT isothermal decay curves, and the X-ray excited integrated emission intensities from 300 to 800 nm as a function of time were recorded by a facility. The facility contains a R928P photomultiplier (Hamamatsu Ltd.), a cryostat in the temperature range between 100 and 723 K, a Hg lamp, and a 50 kV TUB00083-2 X-ray tube (MOXTEK, Ltd.). For optically stimulated TL measurements, different light sources of a near-infrared 850 nm laser, a red 656 nm laser, a commercial White-LED (WLED), a ≈396 nm LED, and a ≈365 nm UV lamp were used. Prior to all TL measurements, all samples have been heated to ≈450 °C for ≈180 s to remove trapped charge carriers from traps and then cooled to 100 K or RT. The TL glow intensities were corrected by both the sample mass and the X-ray or 254 nm UV-light illumination time.

To study charge carrier trapping processes, the thermoluminescence excitation (TLE) curves were measured with an Edinburgh FLS920 fluorescence spectrometer.[21] The Bi^{3+} and/or lanthanides doped $LiTaO_3$ afterglow phosphors were first charged by different energy photon in the wavelength range between 200 and 400 nm for 60 s, and then RT isothermal afterglow decay curves were recorded for 60 s by monitoring the typical emissions of Bi^{3+} at 437 nm, Tb^{3+} at 544 nm, or Pr^{3+} at 614 nm. The integrated RT isothermal afterglow intensities from 0 to 60 s were corrected by the wavelength-dependent excitation intensities of the used xenon lamp in FLS920 spectrometer. A so-called thermoluminescence excitation (TLE) curve like in Figure 6 was established by displaying the corrected afterglow intensities as a function of charging photon wavelength in the spectral range between 200 and 400 nm.

Supporting Information

Supporting Information is available from the Wiley Online Library or from the author.

Acknowledgements

T.L. thanks the financial support from the National Natural Science Foundation of China (No. 12104170), the Fundamental Research Funds for the Central Universities (No. ZQN-1023), and the Scientific Research Funds of Huaqiao University (No. 21BS106). T.L. also thanks the support from Instrumental Analysis Center of Huaqiao University.

Conflict of Interest

The authors declare no conflict of interest.

Data Availability Statement

The data that support the findings of this study are available on request from the corresponding author. The data are not publicly available due to privacy or ethical restrictions.

Keywords

Bi^{2+}, Bi^{3+}, electron release from Bi^{2+}, mechanoluminescence, VRBE, X-ray imaging

Received: April 29, 2022
Revised: June 10, 2022
Published online:

[1] a) P. Pei, Y. Chen, C. Sun, Y. Fan, Y. Yang, X. Liu, L. Lu, M. Zhao, H. Zhang, D. Zhao, X. Liu, F. Zhang, *Nat. Nanotechnol.* **2021**, *16*, 1011; b) Y. Zhuang, D. Chen, W. Chen, W. Zhang, X. Su, R. Deng, Z. An, H. Chen, R.-J. Xie, *Light: Sci. Appl.* **2021**, *10*, 132; c) T. Lyu, P. Dorenbos, *J. Mater. Chem. C* **2018**, *6*, 369; d) J. Du, A. Feng, D. Poelman, *Laser Photonics Rev.* **2020**, *14*, 2000060; e) J. J. Joos, K. Korthout, L. Amidani, P. Glatzel, D. Poelman, P. F. Smet, *Phys. Rev. Lett.* **2020**, *125*, 033001.
[2] a) T. Lyu, P. Dorenbos, C. Li, S. Li, J. Xu, Z. Wei, *Chem. Eng. J.* **2022**, *435*, 135038; b) T. Lyu, P. Dorenbos, *Chem. Eng. J.* **2019**, *372*, 978; c) J. Du, D. Poelman, H. Lin, *Chem. Eng. J.* **2022**, *431*, 133706; d) S. Liu, N. Mao, Z. Song, Q. Liu, *ACS Appl. Mater. Interfaces* **2022**, *14*, 1496.
[3] a) P. Leblans, D. Vandenbroucke, P. Willems, *Materials* **2011**, *4*, 1034; b) T. Lyu, P. Dorenbos, *Chem. Eng. J.* **2020**, *400*, 124776; c) A. Dobrowolska, A. J. J. Bos, P. Dorenbos, *Phys. Status Solidi RRL* **2019**, *13*, 1800502; d) D. Kulesza, A. J. J. Bos, E. Zych, *Acta Mater.* **2022**, 117852.
[4] M. Thoms, H. von Seggern, A. Winnacker, *Phys. Rev. B* **1991**, *44*, 9240.

[5] D. Van der Heggen, R. Zilenaite, E. Ezerskyte, V. Fritz, K. Korthout, D. Vandenberghe, J. De Grave, J. Garrevoet, L. Vincze, D. Poelman, J. J. Joos, P. F. Smet, *Adv. Funct. Mater.* **2022**, *32*, 2109635.
[6] S. Tian, H. Zhang, X. Yang, L. Yang, Q. Min, H. Ma, X. Yu, J. Qiu, X. Xu, *Chem. Eng. J.* **2021**, *412*, 128695.
[7] J. Xu, S. Tanabe, *J. Lumin.* **2019**, *205*, 581.
[8] L. Li, T. Li, Y. Hu, C. Cai, Y. Li, X. Zhang, B. Liang, Y. Yang, J. Qiu, *Light: Sci. Appl.* **2022**, *11*, 51.
[9] X. Wang, Y. Chen, F. Liu, Z. Pan, *Nat. Commun.* **2020**, *11*, 2040.
[10] T. Lyu, in TU Delft RST/Luminescence Materials, *Doctoral Thesis*, Delft University of Technology, Delft **2020**.
[11] P. Dorenbos, *Phys. Rev. B* **2012**, *85*, 165107.
[12] a) P. Dorenbos, *J. Mater. Chem.* **2012**, *22*, 22344; b) H. Luo, A. J. J. Bos, P. Dorenbos, *J. Phys. Chem. C* **2016**, *120*, 5916.
[13] P. Dorenbos, *J. Lumin.* **2020**, *222*, 117164.
[14] a) K. Van den Eeckhout, P. F. Smet, D. Poelman, *Materials* **2010**, *3*, 2536; b) T. Lyu, P. Dorenbos, *J. Mater. Chem. C* **2018**, *6*, 6240.
[15] R. H. P. Awater, P. Dorenbos, *J. Lumin.* **2017**, *184*, 221.
[16] R. H. P. Awater, P. Dorenbos, *J. Lumin.* **2017**, *188*, 487.
[17] M. Nikl, R. Morlotti, C. Magro, R. Bracco, *J. Appl. Phys.* **1996**, *79*, 2853.
[18] R. Hu, Y. Zhang, Y. Zhao, X. Wang, G. Li, C. Wang, *Chem. Eng. J.* **2020**, *392*, 124807.
[19] a) X. Li, X. Wang, R. Hu, Y. Li, X. Yao, *J. Alloys Compd.* **2022**, *896*, 162877; b) G. Qiu, H. Ye, X. Wang, H. Fang, Y. Li, X. Yao, *Ceram. Int.* **2019**, *45*, 8553.
[20] T. Lyu, P. Dorenbos, L. Canhua, W. Zhanhua, *Laser Photonics Rev.* **2022**, 2200055.
[21] a) A. J. J. Bos, R. M. van Duijvenvoorde, E. van der Kolk, W. Drozdowski, P. Dorenbos, *J. Lumin.* **2011**, *131*, 1465; b) A. Dobrowolska, A. J. J. Bos, P. Dorenbos, *Radiat. Meas.* **2019**, *127*, 106147; c) H. Luo, A. J. J. Bos, P. Dorenbos, *J. Phys. Chem. C* **2017**, *121*, 8760.
[22] a) T. Lyu, P. Dorenbos, *Chem. Mater.* **2020**, *32*, 1192; b) P. Dorenbos, *Opt. Mater.* **2017**, *69*, 8.
[23] a) P. Dorenbos, *ECS J. Solid State Sci. Technol.* **2013**, *2*, R3001; b) J. Ueda, S. Miyano, S. Tanabe, *ACS Appl. Mater. Interfaces* **2018**, *10*, 20652.
[24] G. Gasparotto, S. A. M. Lima, M. R. Davolos, J. A. Varela, E. Longo, M. A. Zaghete, *J. Lumin.* **2008**, *128*, 1606.
[25] a) P. Dorenbos, *Opt. Mater.* **2019**, *91*, 333; b) P. Boutinaud, M. Bettinelli, F. Diaz, *Opt. Mater.* **2010**, *32*, 1659.
[26] C. Liu, F. Pan, Q. Peng, W. Zhou, R. Shi, L. Zhou, J. Zhang, J. Chen, H. Liang, *J. Phys. Chem. C* **2016**, *120*, 26044.
[27] P. Dorenbos, *J. Lumin.* **2019**, *214*, 116536.
[28] P. Dorenbos, *ECS J. Solid State Sci. Technol.* **2021**, *10*, 086002.
[29] Y. Zhuang, D. Tu, C. Chen, L. Wang, H. Zhang, H. Xue, C. Yuan, G. Chen, C. Pan, L. Dai, R.-J. Xie, *Light: Sci. Appl.* **2020**, *9*, 182.
[30] a) J.-C. Zhang, X. Wang, G. Marriott, C.-N. Xu, *Prog. Mater. Sci.* **2019**, *103*, 678; b) D. Tu, C.-N. Xu, S. Kamimura, Y. Horibe, H. Oshiro, L. Zhang, Y. Ishii, K. Hyodo, G. Marriott, N. Ueno, X.-G. Zheng, *Adv. Mater.* **2020**, *32*, 1908083; c) C.-N. Xu, T. Watanabe, M. Akiyama, X.-G. Zheng, *Appl. Phys. Lett.* **1999**, *74*, 2414.